

Ambiguous Resonances in Multipulse Quantum Sensing with Nitrogen Vacancy Centers

Lucas Tsunaki,¹ Anmol Singh,¹ Kseniia Volkova,¹ Sergei Trofimov,¹
Tommaso Pregnolato,^{2,3} Tim Schröder,^{2,3} and Boris Naydenov^{1,4,*}

¹*Department Spins in Energy Conversion and Quantum Information Science (ASPIN),
Helmholtz-Zentrum Berlin für Materialien und Energie GmbH, Hahn-Meitner-Platz 1, 14109 Berlin, Germany*

²*Department of Physics, Humboldt-Universität zu Berlin, Newtonstraße 15, 12489 Berlin, Germany*

³*Ferdinand-Braun-Institut (FBH), Gustav-Kirchhoff-Straße 4, 12489 Berlin, Germany*

⁴*Berlin Joint EPR Laboratory, Fachbereich Physik,
Freie Universität Berlin, 14195 Berlin, Germany*

Dynamical decoupling multipulse sequences can be applied to solid state spins for sensing weak oscillating fields from nearby single nuclear spins. By periodically reversing the probing system's evolution, other noises are counteracted and filtered out over the total evolution. However, the technique is subject to intricate interactions resulting in additional resonant responses, which can be misinterpreted with the actual signal intended to be measured. We experimentally characterized three of these effects present in single nitrogen vacancy centers in diamond, where we also developed a numerical simulations model without rotating wave approximations, showing robust correlation to the experimental data. Regarding centers with the ¹⁵N nitrogen isotope, we observed that a small misalignment in the bias magnetic field causes the precession of the nitrogen nuclear spin to be sensed by the electronic spin of the center. Another studied case of ambiguous resonances comes from the coupling with lattice ¹³C nuclei, where we reconstructed the interaction Hamiltonian based on echo modulation frequencies and used this Hamiltonian to simulate multipulse sequences. Finally, we also measured and simulated the effects from the free evolution of the quantum system during finite pulse durations. Due to the large data volume and the strong dependency of these ambiguous resonances with specific experimental parameters, we provide a simulations dataset with a user-friendly graphical interface, where users can compare simulations with their own experimental data for spectral disambiguation. Although focused with nitrogen vacancy centers and dynamical decoupling sequences, these results and the developed model can potentially be applied to other solid state spins and quantum sensing techniques.

I. INTRODUCTION

The second quantum revolution is driving sensing technology [1] to ever-increasing precision and accuracy, thus opening doors to novel measurement possibilities [2–5], reaching the detection of single nuclear spins at room temperature [6–9]. This quantum sensing advantage relies on the fact that quantum properties are extremely sensitive to their environment, which contrarily is a main obstacle for quantum computing — the issue of decoherence [10]. However, such key element is also a vulnerability, as quantum sensors are susceptible to complex interactions with their environment, leading to responses that can be misinterpreted with the actual signal intended to be measured.

In this study, we consider these ambiguous resonant responses which affect multipulse dynamical decoupling (DD) pulse sequences. The technique consists in applying repeated periodic reversals of the quantum evolution of the system, such that dephasings from the environment are counteracted over the entire time evolution. The simplest possible decoupling sequence, known as Hahn echo [11], consists of a single π -pulse between two free-evolutions with same duration $[\tau - \pi - \tau]$, being originally

developed as a way to extend coherence of spin ensembles in nuclear magnetic resonance (NMR). The Hahn echo decay signal can already be used to sense coupled spins [12], however as the number of pulses and free evolution is extended (CPMG sequence [13]), the sequence acts as a narrow frequency or time period filter which cancels out AC signals, except for the frequency corresponding to double of the pulse separation $f_0 = 1/(2\tau)$ and odd fractions of it [14–16]: $f_0/3, f_0/5, f_0/7\dots$ Beyond the Hahn echo and CPMG sequences, a further improvement can be made by intercalating π -pulses over the x and y axes to decouple noises acting on the two different axes. One of these is the XY8- M sequence, with eight $\pi_{x,y}$ -pulses repeated M times as schematically represented in Fig. 1. By decoupling noises acting on different axes, weak signals from single nuclear spins can be filtered from much stronger background fields [6–8], representing a remarkable improvement compared to conventional NMR, which requires large nuclear ensembles and much stronger bias magnetic fields. This improvement come at the expense that the probing system is now intrinsically non-classical, hence having knowledge of its time evolution is indispensable for the resonant signal analysis. To overcome these challenges, an in-depth characterization of such ambiguous resonances experienced by the quantum sensor is necessary for the continued development of the field.

* boris.naydenov@helmholtz-berlin.de

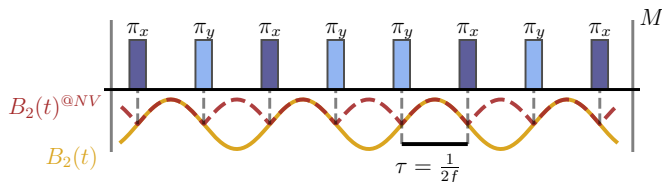


FIG. 1. The XY8- M dynamical decoupling sequence is composed of eight alternated $\pi_{x,y}$ -pulses repeated M times, which counteracts oscillating magnetic field noises except for frequencies corresponding to half of the pulse separation $f_0 = 1/(2\tau)$ and odd fractions of it. This way, it can be applied in a probing spin to sense weak oscillating fields from single nuclear spins.

Quantum sensing DD techniques could in principle be applied to any two-level quantum system. Nonetheless, they excel with color center defects in solids [17], given their versatility to sense different physical quantities and relative ease of experimental realization. Among them, the nitrogen vacancy (NV) center in diamonds has been an epicenter of research due to its remarkable properties at a large range of temperatures and compatibility with biological systems [18, 19], unlike for instance, superconducting quantum interference devices (SQUIDs) [20]. An NV center is a substitutional defect in the diamond lattice where a carbon atom is replaced by nitrogen ^{14}N ($I^n = 1$) or ^{15}N ($I^n = 1/2$) adjacent to a vacancy [Fig. 2 (a)]. The center can accept an extra electron from the lattice, acquiring a negative charge state NV^- and forming a spin triplet ($S = 1$) or singlet ($S = 0$) configuration with the unpaired valence electron of the nitrogen, resulting in well-defined quantum states within the bandgap of diamond [Fig. 2 (b)]. Since our work is concerned with NV^- centers, in the following we denote them as NV for simplicity.

The ground triplet states ^3A can be driven to the excited ^3E states with a non-resonant green laser excitation via the phonon side band. Which then leads to a polarization of the electronic spin state m_s by an optical pumping mechanism via the singlet metastable states, with a preferential decay to $m_s = 0$ [21]. Based on the same mechanism, the resulting fluorescence can be used to resolve the population difference between $m_s = 0$ and $m_s = \pm 1$, since the latter fluoresce less intensively. Finally, transitions between $m_s = 0$ and $m_s = \pm 1$ levels of the ground triplet states ^3A can be coherently driven by resonant microwaves (MW) with controllable duration and phase [22]. This way, a DD sequence consists of three parts: laser initialization, MW manipulation and fluorescence readout. For NVs, $\pi/2$ -pulses are also included before and after DD sequences, in order to drive the electronic spin to and from the plane perpendicular to the quantization axis.

In the context of single NV multipulse sequences, ambiguous resonances can arise from different factors. We begin with Sec. II giving a general theoretical framework used in our simulations, following up with a description of

the experimental and simulation methods in Sec. III. We then discuss each ambiguous resonance: external magnetic field misalignment and hyperfine interaction with ^{15}N nuclei (Sec. IV), coupling with lattice ^{13}C having $I^c = 1/2$ (Sec. V) and free evolution of the system during finite pulses duration [16] (Sec. VI). In sight of the numerous possible ambiguous resonances specific to experimental parameters, we conclude with Sec. VII providing a dataset with graphical interface where simulations can be visualized and compared with the user's experimental data for spectral disambiguation of resonances. Although the discussion is focused on NVs, some of these effects are also relevant to other color centers and quantum systems in general.

II. THEORETICAL FRAMEWORK

Differently from conventional NMR, in DD quantum sensing, the probing system is an inseparable part from the target spin and the exact Hamiltonian of the quantum sensor needs to be taken into account. The total Hamiltonian of a NV in a multipulse sequence can be decomposed in three parts as $H = H_0 + H_1(t) + H_2(t)$, where H_0 is the internal component, $H_1(t)$ is the control Hamiltonian describing the interaction with the MW pulses and $H_2(t)$ the sensing interaction itself. For the first internal component, we consider a model of the ground state triplet, already extensively studied and characterized [23–25]. It can be expressed in the Hilbert space of the electronic and nitrogen nuclear spins $\mathcal{H}_S \otimes \mathcal{H}_{I^n}$ in factors of decreasing energy as

$$H_0 = D \left(S_z^2 - \frac{S^2}{3} \right) + E (S_x^2 - S_y^2) \quad (1.1)$$

$$+ \gamma^e \vec{B}_0 \cdot \vec{S} \quad (1.2)$$

$$+ a_{\perp}^n (S_x I_x^n + S_y I_y^n) + a_{\parallel}^n S_z I_z^n \quad (1.3)$$

$$- \gamma^n \vec{B}_0 \cdot \vec{I}^n, \quad (1.4)$$

where the z axis is taken along the NV axis. The first line (Eq. 1.1) corresponds to the zero-field splitting due to the dipolar interaction between the two electrons, where $D = 2.87$ GHz is the axial component. The parameter E is the off-axis component and is typically negligible, except in nanodiamonds where the crystal strain is significant [25]. The second and fourth lines (Eqs. 1.2 and 1.4) correspond to Zeeman interactions with the external magnetic field \vec{B}_0 for the electronic spin and nitrogen nuclear spin respectively, with gyromagnetic ratios $\gamma^e = 28025$ MHz/T, $\gamma^n = -4.316$ MHz/T for ^{15}N and $\gamma^n = 3.077$ MHz/T for ^{14}N . Here we consider a general case where \vec{B}_0 is not necessarily aligned with the NV axis, as usually assumed. The third line (Eq. 1.3) is the hyperfine interaction between spins which is diagonal in this symmetry referential, with $a_{\perp}^n = -2.70$ MHz and $a_{\parallel}^n = -2.14$ MHz for ^{14}N , while $a_{\perp}^n = 3.65$ MHz and $a_{\parallel}^n = 3.03$ MHz for ^{15}N . When considering ^{14}N , there

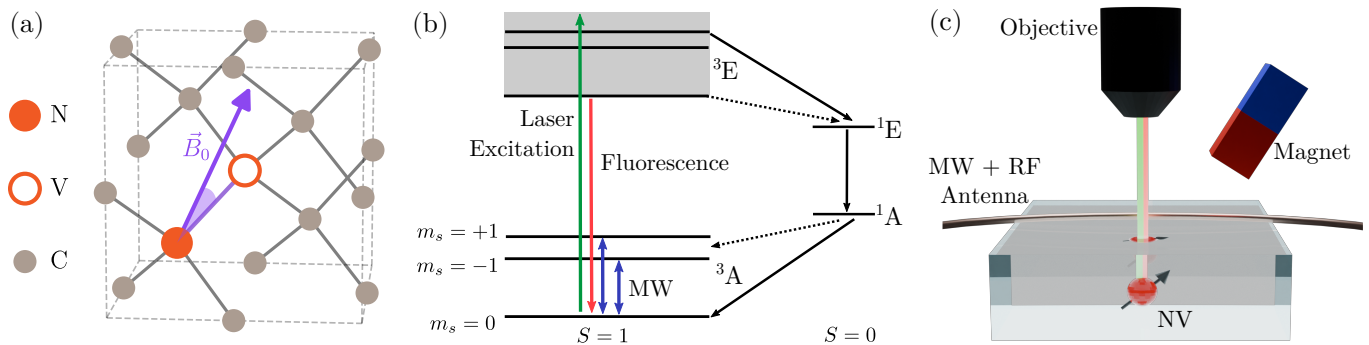


FIG. 2. (a) The NV center is composed of a nitrogen substitution adjacent to a vacancy in the carbon lattice of diamonds. In general, the external magnetic field \vec{B}_0 forms an angle θ_0 with the NV axis. ^{13}C isotopes with spin $1/2$ can also be present near the center. (b) Energy level scheme of NV^- . The electronic spin can be initialized to $m_s = 0$ by optical pumping with green laser, while the state population can be measured by the resulting red fluorescence. Coherent control between $m_s = 0 \leftrightarrow \pm 1$ states is achieved with resonant microwave pulses. (c) Schematic representation of the experimental setup. An air objective focuses the green laser on a single NV, which is also used to collect its red fluorescence. The bias magnetic field \vec{B}_0 is applied with a permanent magnet, while microwave pulses and radio signals are transmitted through a wire on top of the diamond.

is an extra quadrupole term given by $Q(I_z^n)^2$, where $Q = -5.01$ MHz. Although small, the presence of the quadrupole interaction fundamentally changes the dynamics of the system depending on the nitrogen isotope, as the interaction tends to fix the nuclear spin orientation and suppress the Larmor precession of ^{14}N nuclear spins for magnetic fields $B_0 \ll Q/\gamma^n = 1.63$ T [12].

Considering the control Hamiltonian $H_1(t)$, for an oscillating field along a vector \vec{B}_1 , with angular frequency Ω_{MW} and phase ϕ_1 , it can be described as

$$H_1(t) = \gamma^e \sin(\Omega_{MW}t + \phi_1) \vec{B}_1 \cdot \vec{S}. \quad (2)$$

Typically, a rotating wave approximation (RWA) is assumed [26]. Thus, by setting the pulse frequency in resonance with one of the $m_s = 0 \leftrightarrow \pm 1$ transitions, $H_1(t)$ can be treated as a time independent operator which induces a rotation on the Bloch sphere of the respective manifold, where the pulse duration controls the angle and ϕ_1 the axis of rotation in the rotating frame. Although this approximation often results in accurate descriptions of the electronic states transitions, it can overlook important interactions which lead to the ambiguous resonant responses. In particular, the $S_{x,y}$ components of the electronic Zeeman and the perpendicular terms of the hyperfine interactions $a_{\perp}^n (S_x I_x^n + S_y I_y^n)$ do not commute with the rotation operator and result in extra resonance peaks (Sec. IV). This time dependency resulting from the non-commuting terms could still be handled as a perturbation to the secular part of the Hamiltonian up to 2nd order of the dominant term $(1/D)^p$ [12, 27, 28]. However, this approach is also limited, as it overlooks the possibility of double quantum transitions caused by multi-frequency or broad band excitations [29], as well as implies small bias fields $|\gamma_e \vec{B}_0| \ll D$ and weak driving regimes $\gamma_e B_1 \ll D$, which is not always experimentally desired due to extended pulse durations [30]. Furthermore, perturbation theory, in such circumstances, restricts on calculating ap-

proximated eigenvalues for the perturbed Hamiltonian, ignoring exact characteristics of the MW field and the free-evolution of the system during finite pulse durations. Which also leads to other ambiguous resonances (Sec. VI) [16].

For a single nuclear spin in the strong coupling regime but without contact term [9], the sensing Hamiltonian H_2 can be simply expressed in an extended Hilbert space to include the sensed target spin $\mathcal{H}_S \otimes \mathcal{H}_{I^n} \otimes \mathcal{H}_{I^t}$. For $I^t = 1/2$ and neglecting the interaction between the nitrogen and target nuclear spin, this Hamiltonian is given by a hyperfine coupling between the electronic spin operator and the nuclear spin \vec{I}^t added to the Zeeman interaction with the external magnetic field

$$H_2 = \vec{S} \cdot A^t \cdot \vec{I}^t - \gamma^t \vec{B}_0 \cdot \vec{I}^t. \quad (3)$$

Diagonalizing the total Hamiltonian $H_0 + H_2$ results in distinct target nuclear spin Larmor frequencies $\tilde{\omega}_{n_s}^t$, dependent on the electronic spin state. Given that the hyperfine matrix A^t must be symmetrical, the sensing interaction is completely described by its six components plus the gyromagnetic ratio γ^t . The same Hamiltonian can also be used to describe an ensemble of nuclear spins, provided that their states are represented by density operators. Apart from nuclear spins, it is also desirable to sense oscillating classical fields. Particularly for this study, an externally applied RF signal has the advantage of having controllable intensity and frequency. In this case, the interaction is described in terms of a field $\vec{B}_2(t)$ with frequency f_0 as

$$H_2(t) = \gamma^e \sin(2\pi f_0 t + \phi_2) \vec{B}_2 \cdot \vec{S}, \quad (4)$$

in analogy to Eq. 2.

In a simplified manner, an ensemble of nuclear spins could also be thought of in terms of a semi-classical oscillating field [9, 31]. Despite their average magnetization

being close to zero at room temperature, their collective precession around \vec{B}_0 results in an effective oscillating magnetic field with statically varying amplitude and phase, but with frequencies centered around the effective nuclear Larmor frequencies $\tilde{\omega}_{m_s}^t$ at each electronic state m_s . On the other hand, a weak classical RF signal could emulate a precessing nuclear spin and be approximately described in terms of an effective hyperfine interaction. Hence, an analogy can be drawn between the quantum and semi-classical descriptions from Eqs. 3 and 4, where the interaction is either represented in terms of the six hyperfine components plus gyromagnetic ratio $\{A_{ij}^c, \gamma^s\}$ or the three nuclear precision frequencies plus four parameters of the effective field vector $\{\tilde{\omega}_{m_s}^t, \phi_2, \vec{B}_2\}$, respectively. Strictly speaking, both Hamiltonians describe fundamentally different processes, yet they share mathematical similarities and can lead to resembling effects at low order XY8- M sequences, as further shown in the Supplementary Materials Sec. S5.

Altogether, a complete description of the pulsed dynamics of the NV subject to a multipulse sequence needs to account for the time-dependent MW pulses and oscillating RF field in the laboratory reference frame, while operating over mixed states. Within these considerations, the time evolution of the system can be solved by the Liouville-von Neumann equation

$$i\hbar\dot{\rho}(t) = [H_0 + H_1(t) + H_2(t), \rho(t)], \quad (5)$$

with $H_1(t)$ being present only during MW pulses but H_0 and $H_2(t)$ during the entire time evolution. This results in a set of coupled differential equations for the elements in the density matrix representing the whole system $\rho(t)$ [32], which can be integrated numerically in discretized small time steps [33, 34]. Another advantage of this method is that the non-unitary dynamics can be easily incorporated with the Lindblad equation [35], using the associated collapse operators of decoherence and relaxation. Lastly, the observable measured after the DD sequence, i.e. the fluorescence, is given by the expectation value of the bright state density operator $p = \text{Tr}[\rho_0 \rho^\dagger(t_f)]$, where ρ_0 is the initial bright state and $\rho(t_f)$ the final state obtained from the equation. As discussed on Sec. I, the electronic spin is optically initialized at $m_s = 0$, while the nitrogen and target nuclear spins are in thermal equilibrium given by the Boltzmann distribution, which at room temperature leads to an identity density matrix. Thus, the initial state considered in the simulations is $\rho_0 \equiv |0\rangle\langle 0| \otimes \mathbb{1} \otimes \mathbb{1}$, where the dimensions of $\mathbb{1}$ dependent on the spin number of the nuclei.

III. EXPERIMENTAL AND SIMULATION METHODS

Experimental data was obtained with a home-built confocal microscope as described in [36] and schematically represented in Fig. 2 (c). Single NVs are addressed with a green laser in continuous or pulsed modes using

an air objective, while their fluorescence is measured by a single photon detector. MW pulses are produced by an arbitrary waveform generator, which are then amplified and transmitted to the diamond by a thin copper wire. RF fields are generated continuously with controllable power and frequency, combined and then transmitted with the MW pulses as well. The external bias magnetic field B_0 is applied with a permanent magnet with four degrees of movement, while its intensity and the angle formed with the NV axis θ_0 are calculated by the asymmetry between peaks in the continuous wave or pulsed optical detected magnetic resonance (ODMR) spectrum [37]. Lastly, the software package Qudi [38] is used for hardware control and data acquisition.

In order to study each ambiguous resonance, different properties were required for the diamond samples. For measuring ^{13}C ambiguous resonances, Sec. V, a CVD grown sample with ^{14}N was chosen in order to avoid ^{15}N effects. Conversely, in Sec. IV, Hahn echo modulations and XY8- M were measured in shallow implanted ^{15}N diamonds. For longer XY8-12 measurements (Sec. VI), a deeper implanted ^{15}N diamond sample was used with longer coherence times. A more detailed description of the experimental setup and diamond samples can be found in Sec. S1 and Sec. S2.

The simulated time evolutions of the pulsed dynamics were calculated using the master equation solver from Quantum Toolbox in Python (QuTiP) [33, 34] in parallel over 64 physical CPU cores. Experimentally measured fluorescence and simulated transition probability are compared through a linear relation, physically representing experimental uncertainties, as the collection efficiency or background light. The correlation r between them is quantified from -1 to 1 by the Pearson coefficient [1], see Sec. S3 for more details. In Sec. VI, where the coupling parameters of H_2 are not defined, the transition probability was simulated over several points in parameter space and the simulation with the highest correlation coefficient was assumed.

IV. MAGNETIC FIELD MISALIGNMENT AND ^{15}N COUPLING

Perfectly aligning the bias field with the NV axis with accuracy much greater than $\Delta\theta_0 = 1^\circ$ requires a precise vector magnet, which is not the case for widely used permanent magnets. In these circumstances, the $S_{x,y}$ Zeeman components and perpendicular nitrogen hyperfine terms can induce undesired electronic spin flips during multipulse sequences. This is better understood in another reference frame where \vec{B}_0 is aligned along the new z axis, causing the nitrogen hyperfine matrix to assume non-diagonal terms just like in the sensing Hamiltonian of Eq. 3. Consequently, the misaligned field can cause the NV's electronic spin to sense its own nitrogen nuclear spin. Although this effect happens with both nitrogen isotopes, for ^{14}N it is nearly negligible at moderate

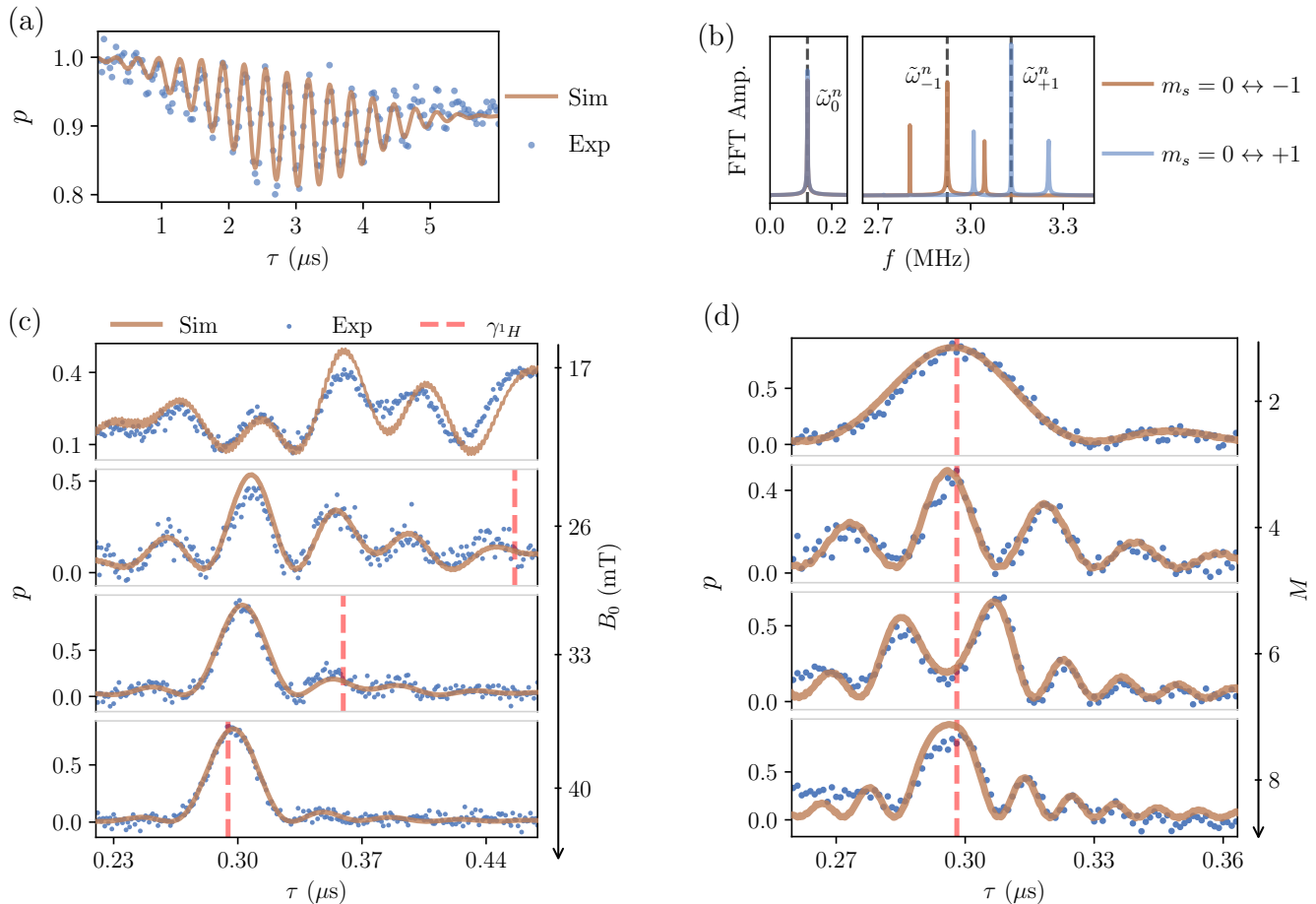


FIG. 3. (a) Experimental and simulated Hahn echo decay for $m_s = 0 \leftrightarrow +1$ transition at $B_0 = 24$ mT and misalignment of $\theta_0 = 2.1^\circ$ with modulations due to ^{15}N interaction with NV electronic spin. The coherence decay is fitted by $\exp[-(t/\tau_c)^4]$ [12] with $\tau_c = 4.018 \pm 0.007 \mu\text{s}$ and correlation $r = 0.934$. (b) FFT of the simulated Hahn echo decay for both $m_s = 0 \leftrightarrow \pm 1$ transitions. The envelope modulations are defined by the effective Larmor frequencies of ^{15}N $\omega_{m_s}^n$, numerically simulated from the Hamiltonian. Less intense sidebands from $\omega_{\pm 1}^n$ are also present in the spectra. (c) Experimental and simulated XY8-2 of the ^{15}N resonances for different values of B_0 with $\theta_0 = (17.0, 9.3, 5.1, 2.7)^\circ$ and correlations $r = (0.858, 0.890, 0.971, 0.986)$, respectively. The resonance peaks have varying amplitude at almost constant pulse separations, evidencing a dominance of the hyperfine interaction with the electronic spin over the Zeeman interaction of the ^{15}N spin with B_0 . The expected resonances from ^1H are also shown at $\tau_H = 1/(2\gamma_H B_0)$. (d) XY8-M at $B_0 = 39$ mT and $\theta_0 = 3.8^\circ$ with $r = (0.975, 0.921, 0.945, 0.906)$, respectively. At this field, the ambiguous resonance could be mistakenly attributed to ^1H nuclear spins. The high correlation between simulations and experimental data for longer pulse sequences further corroborate the numerical model.

fields due to the quadrupole interaction (Sec. II), thus we restrict the discussion to ^{15}NV in this section.

The influence of ^{15}N coupling in simple pulsed experiments is already known, but restricted to a semi-analytical framework [12, 27] under certain approximations, as discussed in Sec. II. Here we show that the measured Hahn echo decay also agrees with our numerical simulation model with a high correlation of $r = 0.934$, Fig. 3 (a). The electronic coherence decay presents envelope modulations with their periods determined by the effective nitrogen Larmor frequencies $\tilde{\omega}_{m_s}^n$, as shown by the fast Fourier transform (FFT) taken from the simulated data, Fig. 3 (b). As the number of pulses is increased however, an analytical approach for solving Eq.

5 and calculating this nitrogen coupling effect becomes increasingly complex.

To study these effects in longer DD sequences, XY8-2 for the $m_s = 0 \leftrightarrow +1$ transition were measured and simulated over a fixed τ range varying the magnetic field amplitude and angle, as shown in Fig. 3 (c). The frequency of nitrogen-related resonances does not depend linearly on the applied magnetic field, as one would expect from a simple Zeeman relation. In contrast, the hyperfine interaction, dominating the energy levels of the nuclei, results in peaks with varying intensity and nearly constant position as the field changes. The peaks positions do not correspond to the effective Larmor frequencies of the nitrogen nuclei $\tilde{\omega}_{m_s}^n$ and a semi-analytical model which de-

scribes their resonant frequency values remains an open problem. The lowest magnetic field shows the worst correlation between experiment and simulation of $r = 0.858$, where a pulse duration error had to be included in the simulation. This causes a fast modulation of the signal, as discussed in details in . The smaller correlation can be attributed to a larger misalignment angle of $\theta_0 = 17.0^\circ$, thus with a larger uncertainty.

These resonances differ in each $m_s = 0 \leftrightarrow \pm 1$ transition due to distinct nuclear state energies and are also present at higher τ given by the odd fractions of their resonant frequencies ($f_0/3, f_0/5, f_0/7\dots$), as previously observed for ^{13}C resonances [6]. At long pulse separations of several μs , they mix and become a near continuum, which can be visualized in the simulations dataset. ^{15}N resonances do not seem to occur at short pulse spacings of about less than 250 ns. Still, short τ are occupied by high frequency noises from paramagnetic impurities and even multiples of the resonant frequencies (Sec. VI) [16]. Moreover, setting the resonant frequencies of target nuclear spins with low gyromagnetic ratios γ^t at $\tau < 250$ ns is technically challenging, as it requires large bias fields B_0 and the capability of amplifying MW fields at a large frequency range of Ω_{MW} (Eq. 2). Thus, these resonances from ^{15}N are just unavoidable in many cases, underlying the necessity for a dataset where users can compare their experimental data for disambiguation. It is important to note, however, that not all ^{15}NV centers under misaligned fields will present these ambiguous resonances, as additional interactions might dominate over it.

Fig. 3 (c) also illustrates how these resonances could be mistakenly attributed to some other nuclei. The ^{15}N resonance is compared with the expected Larmor frequency resonance of the commonly measured ^1H nuclei $\tau_H = 1/(2\gamma^h B_0)$, where $\gamma^h = 42.57$ MHz/T. It can be seen that at 39 mT, the ambiguous resonance closely resembles a ^1H nucleus. In Fig. 3 (d), the signal dependence on the order of the pulse sequence M is shown, while $B_0 = 39$ mT is kept constant. A strong agreement between the experimental data and the simulations is also observed for these longer sequences with many pulses, further corroborating the numerical model.

V. ^{13}C COUPLING

Carbon nuclear isotope ^{13}C with spin-1/2 is present in most diamonds with 1.1% natural abundance, excluding otherwise isotopically purified crystals with increased costs. ^{13}C sensing and manipulation by multipulse sequences is itself an active topic of research in sight of the potential for long-lived quantum memories [6, 40], but in this case, it can act as another source of ambiguous resonances. Compared to ^{15}N in the previous section, the Hamiltonian becomes more complex, as there are six free parameters from the hyperfine interaction A^c in Eq. 3 and off-diagonal terms cannot be assumed null because the reference frame is already being chosen such that \vec{B}_0

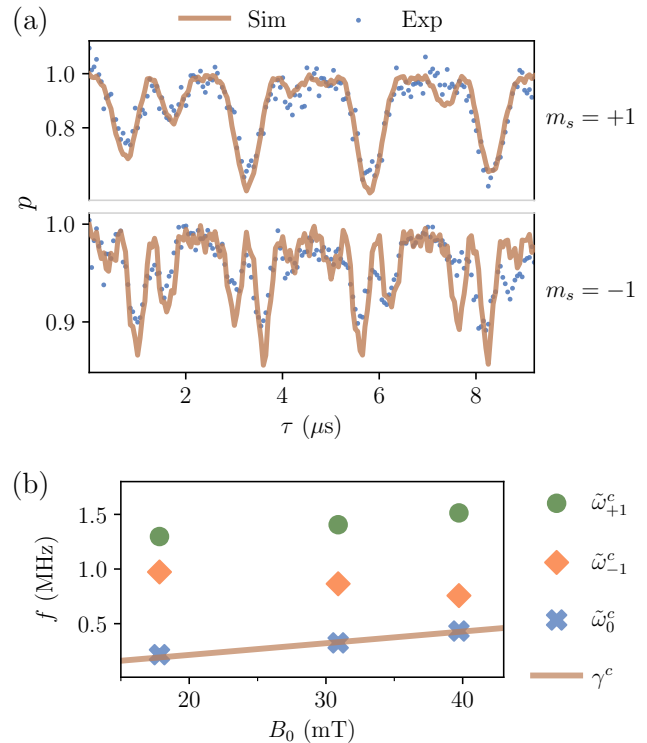


FIG. 4. (a) Hahn echo decays for both $m_s = 0 \rightarrow \pm 1$ transitions of a ^{14}NV coupled to a ^{13}C nuclear spin at $B_0 = 40$ mT. Both transitions show a slow modulation from the $\tilde{\omega}_0^c$ nuclear Larmor frequency at $m_s = 0$ and fast modulations $\tilde{\omega}_{\pm 1}^c$ from the $m_s = \pm 1$ states. Correlations between experimental and simulated data are $r = (0.926, 0.761)$. (b) Modulation frequencies obtained by FFT from the Hahn echo decays as function of B_0 . $\tilde{\omega}_0^c$ is closely related to the bare gyromagnetic ratio of ^{13}C due to an almost zero hyperfine interaction at $m_s = 0$, while $\tilde{\omega}_{\pm 1}^c$ also decreases or increases linearly with an offset given by Eq. 6. Based on the experimental values of these modulations, the hyperfine tensor A^c was determined by comparing them with the calculated eigenvalues from the total Hamiltonian.

lies on the xz plane and the NV axis is along z . Therefore, the initial goal is to determine the hyperfine interaction matrix A^c between a NV and a coupled ^{13}C nucleus, such that the numerical simulations model can be validated with experimental data and subsequently extended to an arbitrary ^{13}C coupling or even other spins.

Similar to the coupling with ^{15}N , the Hahn echo decay of an NV coupled to a ^{13}C nuclear spin is also expected to show periodic oscillations given by the effective Larmor frequencies of the nuclei $\tilde{\omega}_{m_s}^c$ [12]. Thus, Hahn echo was measured in a single NV for both electronic transitions $m_s = 0 \rightarrow \pm 1$ at three different magnetic fields, in a sample with the ^{14}N isotope to avoid nitrogen modulations as in the previous section. The experimentally measured and later simulated modulations at $B_0 = 40$ mT are shown in Fig. 4 (a), where no coherence decay can be observed at this time scale. The Hahn echo for the two

other values of B_0 can be found in Sec. S4. As with ^{15}N coupling, the Hahn echo decay for $m_s = 0 \rightarrow -1$ transition will present a slow modulation from $\tilde{\omega}_0^c$ and a fast one from $\tilde{\omega}_{-1}^c$, similarly to the $m_s = 0 \rightarrow +1$ transition with $\tilde{\omega}_{+1}^c$ begin the fast modulation. The values of the nuclear Larmor frequencies $\tilde{\omega}_{m_s}^c$ obtained from FFT are

plotted against the bias field in Fig. 4 (b). The $\tilde{\omega}_0^c$ frequency is closely related to the bare gyromagnetic ratio of ^{13}C $\gamma^c = 10.705$ MHz/T, because of an almost zero hyperfine interaction at $m_s = 0$. On the other hand, $\tilde{\omega}_{+1}^c$ and $\tilde{\omega}_{-1}^c$ respectively increases or decreases by the same amount based on the sign of m_s and at $B_0 = 0$ mT, both of them are given by [41]

$$\tilde{\omega}_{\pm 1}^c(B_0 = 0) = \sqrt{(A_{zx}^c)^2 + (A_{zy}^c)^2 + (A_{zz}^c)^2}. \quad (6)$$

Finally, several different combinations of the hyperfine elements in Eq. 3 were considered and the eigenvalues of the total Hamiltonian $H_0 + H_2$ calculated numerically. The hyperfine interaction matrix A^c with the least square difference from the experimental values of $\tilde{\omega}_{m_s}^c$ is shown in Sec. S4. Using the obtained A^c , the Hahn echo decay was simulated [Fig. 4 (a)], resulting in the same experimental modulations with high correlations of $r = 0.926$ for $m_s = +1$ and $r = 0.761$ for $m_s = -1$.

Based on the obtained hyperfine interaction matrix, XY8-2 for the $m_s = 0 \rightarrow +1$ transition was simulated and measured at the same bias magnetic fields, as shown in Fig. 5 (a). The numerical simulation model and the calculated A^c accurately describe the resonances induced by the ^{13}C nuclear spin. As B_0 increases, the resonance shifts to shorter pulse separations and faster frequencies. This, in contrast to the coupling with ^{15}N [Fig. 3 (b)], evidences that the Zeeman interaction of the ^{13}C nuclear spin with the external magnetic field is comparable in strength with the hyperfine interaction with the NV. Lastly, Fig. 5 (b) presents XY8- M measured and simulated at $B_0 = 40$ mT. Analogous to the ^{15}N resonance [Fig. 3 (d)], the linewidth becomes narrower and sidebands become more pronounced as the order of the sequence increases, which can be understood in terms of an alteration of the frequency filter function induced by the DD sequence [31].

At the magnetic fields shown here, this NV exhibits ^{13}C resonances which do not overlap with other possible nuclear spin species. However, for different couplings and fields, it may be the case that the interaction with ^{13}C leads to ambiguous resonances with other nuclear species. Given the crystalline periodicity of the host diamond, a ^{13}C atom can only occupy a limited number of lattice sites around the NV, resulting in a discrete set of possible hyperfine coupling strengths divided into families [41–43]. Thus, the dataset provides simulations for hyperfine parameter values calculated from density functional theory [41], such that a few possible ^{13}C resonances can be disambiguated from experimental data at different fields. A more conclusive method to identify the nuclear species giving rise to some resonance is, however, to measure the modulation frequencies on the Hahn echo signal and compare the slow modulation with the expected gyromagnetic ratio, as performed here. Although we focused the discussion on lattice ^{13}C nuclear spins, the same method is applicable to an arbitrary spin coupled to the NV, as long as their interaction can be modeled by Eq. 3.

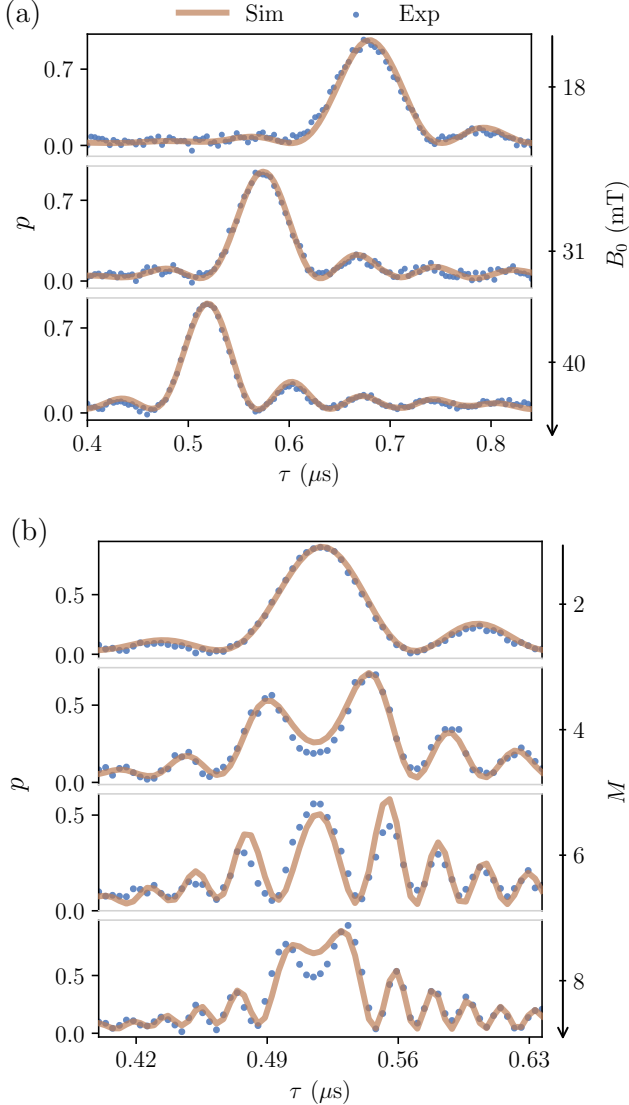


FIG. 5. (a) XY8-2 resonances from a ^{14}NV coupled to a ^{13}C nuclear spin as a function of B_0 for the $m_s = 0 \rightarrow +1$ transition. The calculated hyperfine matrix A^c was used to simulate the resonances, with correlations $r = (0.987, 0.990, 0.989)$. As the magnetic field increases, the resonance shifts to larger frequencies, influenced the positive gyromagnetic ratio of ^{13}C . (b) Simulated and experimental XY8- M at $B_0 = 40$ mT, with correlations $r = (0.989, 0.977, 0.902, 0.951)$. As the order of the sequence increases, sidebands become more pronounced and line-widths smaller. The high correlation between simulations and experiments attests the robustness of the numerical model also on higher dimensional Hilbert spaces, $\mathcal{H}_S \otimes \mathcal{H}_{I^n} \otimes \mathcal{H}_{I^t}$.

VI. FINITE PULSE DURATION

In most applications of multipulse sequences, perfect δ pulses with zero temporal length are assumed. Even though the pulse length might still be much smaller than the pulse separation $t_\pi \ll \tau$, it has been shown that the free evolution of the system during finite pulse durations under the influence of H_0 leads to additional resonances at even multiples of the resonant frequencies and their odd subharmonics [16], that is $f = 2k/(2l + 1)f_0$ for k and l natural. Notably, lattice ^{13}C nuclear spins can give rise to ambiguous resonances of ^1H , other than the ones already described in the previous section. This occurs because the 4th harmonic of a weakly coupled ^{13}C coincides with the fundamental resonance of ^1H , given that $4\gamma^c = 42.82$ MHz/T and $\gamma^h = 42.57$ MHz/T. These ambiguous resonances can still be greatly suppressed by adding a random phase Φ_m for each $\text{XY}8_m$ block, known as the $\text{RXY}8$ - M sequence [2, 45]. A further improvement of this suppression was theoretically proposed by correlating the random phases such that they cancel each other every g repetitions of the $\text{XY}8$ block, $\sum_m^g \exp(-i\Phi_m) = 0$ [3].

To experimentally reproduce these ambiguous resonances, an external RF signal with frequency $f_0 = 5.5$ MHz was applied to a single NV at bias field $B_0 = 38$ mT and π -pulse length $t_\pi = 17.16$ ns. Four different multipulse sequences were applied as shown in Fig. 6. In all four we observe multiple fringes around the fundamental resonance $\tau_0 = 1/(2f_0)$, resulting from the convolution of the spectral density of the RF field and the filter function of the multipulse sequence [31]. Apart from that, $\text{XY}8$ -12 has four of these ambiguous resonances at $f/f_0 = 2/3, 4/3, 4/5$ and $4/7$, which are already greatly suppressed with $\text{RXY}8$ -12. We also demonstrate the experimental realization of $\text{RXY}8$ -12 with correlated phases at $g = 2$ and $g = 3$ repetitions, with no noticeable differences from uncorrelated $\text{RXY}8$ at these experimental conditions. Another advantage of introducing the random phase Φ_m lies in the robustness against pulse errors [3], such as in the pulse length and detuning of the MW resonant frequency. These lead to a degradation of the resonance contrasts and are discussed in more details in SM:V.

Eq. 4 was used to model the RF interaction with the NV, with the best correlations found for $\gamma_e B_2^z = 0.28$ MHz and $\gamma_e B_2^x = \gamma_e B_2^y = 0$. The simulations also show a suppression of the spurious harmonics by the phase randomization. Hence, demonstrating that the numerical simulations model can be applied for time-dependent sensing Hamiltonians $H_2(t)$, while also taking into account the specific time dependency of the control Hamiltonian $H_1(t)$ from Eq. 2.

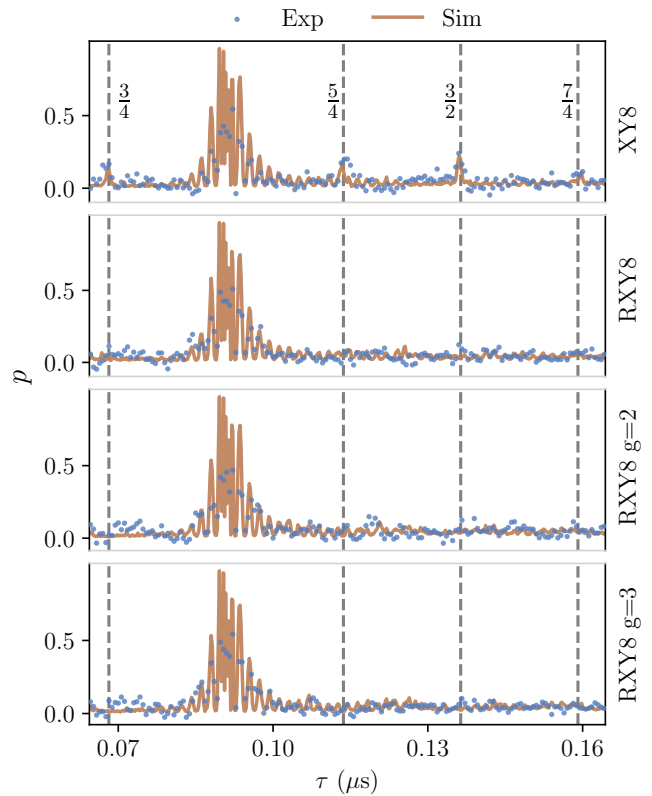


FIG. 6. $\text{XY}8$ -12 and $\text{RXY}8$ -12 sequences with resonance from an external RF signal with $f_0 = 5.5$ MHz for $m_s = 0 \leftrightarrow -1$ transition. Multiple fringes are observed around the fundamental resonance $\tau_0 = 1/(2f_0)$, in addition, spurious harmonics at $\tau_0/\tau = 3/4, 5/4, 3/2$ and $7/4$ are suppressed by the phase randomization. Random phase correlations with $g = 2$ and 3 are also demonstrated, without much differences from uncorrelated $\text{RXY}8$. The best correlations $r = (0.839, 0.877, 0.818, 0.888)$ occur at $\gamma_e B_2^z = 0.28$ MHz and $\gamma_e B_2^x = \gamma_e B_2^y = 0$ from Eq. 4.

VII. DISCUSSION AND SIMULATIONS DATASET

Noise filtering by DD sequences has proven to be an effective technique in quantum sensing, capable of detecting very weak oscillating fields of even single nuclear spins. This great sensitivity comes at the cost of an often complex signal analysis influenced by external and inherent interactions which lead to ambiguous resonances, such as the ones studied in this paper. It is therefore imperative that these effects are well understood and characterized for an accurate identification of nuclear spin resonances. Among candidate platforms, the NV center in diamonds outstands in its ease of implementation and versatility with different biological and chemical systems. Nevertheless, widely adopted approximations and oversimplifications of the system dynamics completely overlook these ambiguous resonances. Examples of such approximations are the RWA, assuming per-

fect δ -pulses, adopting a reduced electronic spin manifold where $S = 1/2$ or ignoring the nitrogen nuclear spin of the center.

In this paper, we proposed a numerical simulations model for the time-dependent dynamics of the NV under a DD sequence and experimentally characterized three effects that lead to ambiguous resonances. Where in all three cases, the numerical simulations model showed robust correlations with the experimental data. Regarding ^{15}N , a small misalignment of the bias magnetic field gives rise to non-commuting elements with the rotation operator of the RWA. Which in turn, can cause the precession of ^{15}N nuclear spins to be sensed via the hyperfine interaction. These resonances are present for pulse separations $\tau > 250$ ns and differ depending on the m_s state. The small sensitivity of the resonant frequencies with the magnetic field B_0 evidences the dominance of the hyperfine interaction with the electronic spin, over the Zeeman interaction with B_0 . We have also shown that in the presence of an external misaligned field around 40 mT, the ^{15}N resonances closely resemble those from ^1H nuclear spin for different XY8- M orders. This characterization of ^{15}N resonances provides a basis for future studies aimed at using the ^{15}N nuclear spin as a quantum memory [6, 40].

Another more studied source of ambiguous resonances are the diamond lattice ^{13}C nuclear spins, which can also couple to the NV electronic spin with resonant frequencies depending on the hyperfine interaction matrix A^c . Here, we have presented a method for unequivocally calculating A^c , based on the Hahn echo decay modulation frequencies as a function of the bias field B_0 . Followed by a comparison with numerically calculated eigenvalues from the total Hamiltonian. The method is further validated by the XY8- M measurements and simulations at different fields and orders. This also demonstrates that the numerical simulation model can be applied to higher dimensional Hilbert spaces, in this case including the sensed spin. Although applied for ^{13}C nuclear spins, the method is general to any coupled spins in the strong coupling regime [9], as long as they can be described in terms of a Hamiltonian as in Eq. 3.

Specific parameters of the MW control pulses which are not accounted for in perturbation theory also affect the resonances of DD sequences. In particular, the free evolution of the probing spin during finite pulse durations leads to resonances at the even multiples of the fundamental resonant frequencies [16]. These resonances, however, can be suppressed with a phase randomization in each XY8 block [2, 45]. In this paper, we experimentally demonstrated the RXY8 with random phase correlation, which has been proposed to further improve spurious harmonics suppression and robustness against pulse errors [3]. The capability of the simulations model to account for the specific time-dependency of the control field $H_1(t)$, Eq. 2, further underlines its versatility.

Unlike the ambiguous resonances originating from the finite pulse durations, a straightforward method for sup-

pressing the resonances from ^{15}N and ^{13}C in DD sequences remains an open problem. Currently, this would involve more elaborate experimental conditions, as precise vector magnets, isotopically purified diamonds or more complicate pulse sequences. Therefore, some of the ambiguous resonances presented here are unavoidable in a large variety of experiments. A platform for analyzing and identifying spectral features is thus essential for the continued development of the field, as these ambiguous resonances are largely dependent on specific experimental parameters, resulting in numerous possible resonant responses in multipulse DD sequences.

To further extend the toolbox of available methods, we provide a dataset comprised of around 10^4 simulations of XY8- M for ^{15}N and ^{13}C ambiguous resonances. Both m_s transitions were considered with several different combinations of B_0 and order M . It is important to note however, that a fixed Rabi frequency of $\gamma_e B_1 = 40$ MHz was considered in all simulations, which may lead to slight differences at high order XY8. For ^{15}N resonances, the angle θ_0 was also changed, whereas for ^{13}C , the hyperfine matrices of all provided families [41] were considered. The simulations can be visualized and compared with the user's experimental data for spectral disambiguation through a user-friendly graphical interface, published under DOI:10.6084/m9.figshare.26245895 [47], where a complete guide for installation and usage are also provided. Even though the dataset only contains XY8- M simulations for NVs so far, it can be used for other DD sequences which have similar resonance spectra, such as the CPMG [13]. Furthermore, the model and results here presented have the potential to be extended to other color centers or quantum systems in general, as well as to more elaborate DD sensing protocols.

ACKNOWLEDGMENTS

We acknowledge Miriam Mendoza Delgado and Prof. Dr. Cyril Popov from the Institute of Nanostructure Technologies and Analytics of the University of Kassel for the annealing a diamond sample. We are also grateful to Karolina Schüle, Jens Fuhrmann and Prof. Dr. Fedor Jelezko from the Institute for Quantum Optics of Ulm University for providing another diamond sample. Finally, we would like to thank Alexander Külberg and Dr. Andreas Thies from Ferdinand-Braun-Institute (FBH) for performing the ion implantations. This work was supported by the German Federal Ministry of Education and Research (BMBF) under the Grand Challenge of Quantum Communication, in a collaboration between "Diamant-basiert QuantenTOKen" (DIQTOK - n° 16KISQ034) and "Quantum Photonic Integrated Scalable memory" (QPIS - n° 16KISQ032K) projects. In addition, this work received funding from BMBF project DiNOQuant (No. 13N14921) and German Research Foundation (DFG) grants 410866378 and 41086656.

DATA & CODE AVAILABILITY

All data and code used in this work are available for scientific use upon reasonable request.

-
- [1] C. L. Degen, F. Reinhard, and P. Cappellaro, Quantum sensing, *Rev. Mod. Phys.* **89**, 035002 (2017).
- [2] B. P. Abbott *et al.*, Gw150914: The advanced ligo detectors in the era of first discoveries, *Phys. Rev. Lett.* **116**, 131103 (2016).
- [3] S. Chen *et al.*, Immunomagnetic microscopy of tumor tissues using quantum sensors in diamond, *Proceedings of the National Academy of Sciences* **119**, e2118876119 (2022).
- [4] N. Aslam *et al.*, Quantum sensors for biomedical applications, *Nature Reviews Physics* **5**, 157 (2023).
- [5] M. Fujiwara, S. Sun, A. Dohms, Y. Nishimura, K. Suto, Y. Takezawa, K. Oshimi, L. Zhao, N. Sadzak, Y. Umehara, Y. Teki, N. Komatsu, O. Benson, Y. Shikano, and E. Kage-Nakadai, Real-time nanodiamond thermometry probing in vivo thermogenic responses, *Science Advances* **6**, eaba9636 (2020).
- [6] T. H. Taminiiau, J. J. T. Wagenaar, T. van der Sar, F. Jelezko, V. V. Dobrovitski, and R. Hanson, Detection and control of individual nuclear spins using a weakly coupled electron spin, *Phys. Rev. Lett.* **109**, 137602 (2012).
- [7] P. Neumann, J. Beck, M. Steiner, F. Rempp, H. Fedder, P. Hemmer, and F. Jelezko, Single-shot readout of a single nuclear spin, *Science* **329**, 542 (2010).
- [8] L. Childress, M. V. G. Dutt, J. M. Taylor, A. S. Zibrov, F. Jelezko, J. Wrachtrup, P. R. Hemmer, and M. D. Lukin, Coherent dynamics of coupled electron and nuclear spin qubits in diamond, *Science* **314**, 281 (2006).
- [9] C. Müller, X. Kong, J.-M. Cai, K. Melentijević, A. Stacey, M. Markham, D. Twitchen, J. Isoya, S. Pezzagna, J. Meijer, *et al.*, Nuclear magnetic resonance spectroscopy with single spin sensitivity, *Nature communications* **5**, 4703 (2014).
- [10] M. Schlosshauer, Quantum decoherence, *Physics Reports* **831**, 1 (2019).
- [11] E. L. Hahn, Spin echoes, *Phys. Rev.* **80**, 580 (1950).
- [12] L. Childress, M. V. G. Dutt, J. M. Taylor, A. S. Zibrov, F. Jelezko, J. Wrachtrup, P. R. Hemmer, and M. D. Lukin, Coherent dynamics of coupled electron and nuclear spin qubits in diamond, *Science* **314**, 281 (2006).
- [13] S. Meiboom and D. Gill, Modified spin-echo method for measuring nuclear relaxation times, *Review of Scientific Instruments* **29**, 688 (2004).
- [14] B. Naydenov, F. Dolde, L. T. Hall, C. Shin, H. Fedder, L. C. L. Hollenberg, F. Jelezko, and J. Wrachtrup, Dynamical decoupling of a single-electron spin at room temperature, *Phys. Rev. B* **83**, 081201 (2011).
- [15] G. de Lange, D. Ristè, V. V. Dobrovitski, and R. Hanson, Single-spin magnetometry with multipulse sensing sequences, *Phys. Rev. Lett.* **106**, 080802 (2011).
- [16] M. Loretz, J. M. Boss, T. Rosskopf, H. J. Mamin, D. Rugar, and C. L. Degen, Spurious harmonic response of multipulse quantum sensing sequences, *Phys. Rev. X* **5**, 021009 (2015).
- [17] R. J. D. Tilley, Color centers, in *Encyclopedia of Color Science and Technology*, edited by R. Luo (Springer New York, New York, NY, 2014) pp. 1–9.
- [18] E. V. Levine, M. J. Turner, P. Kehayias, C. A. Hart, N. Langellier, R. Trubko, D. R. Glenn, R. R. Fu, and R. L. Walsworth, Principles and techniques of the quantum diamond microscope, *Nanophotonics* **8**, 1945 (2019).
- [19] S. Pezzagna and J. Meijer, Quantum computer based on color centers in diamond, *Applied Physics Reviews* **8**, 011308 (2021).
- [20] R. L. Fagaly, Superconducting quantum interference device instruments and applications, *Review of Scientific Instruments* **77**, 101101 (2006).
- [21] A. Gruber, A. Dräbenstedt, C. Tietz, L. Fleury, J. Wrachtrup, and C. von Borczyskowski, Scanning confocal optical microscopy and magnetic resonance on single defect centers, *Science* **276**, 2012 (1997).
- [22] F. Jelezko, T. Gaebel, I. Popa, A. Gruber, and J. Wrachtrup, Observation of coherent oscillations in a single electron spin, *Phys. Rev. Lett.* **92**, 076401 (2004).
- [23] J. H. N. Loubser and J. A. van Wyk, Electron spin resonance in the study of diamond, *Reports on Progress in Physics* **41**, 1201 (1978).
- [24] M. W. Doherty, N. B. Manson, P. Delaney, F. Jelezko, J. Wrachtrup, and L. C. Hollenberg, The nitrogen-vacancy colour centre in diamond, *Physics Reports* **528**, 1 (2013).
- [25] L. Rondin, J.-P. Tetienne, T. Hingant, J.-F. Roch, P. Maletinsky, and V. Jacques, Magnetometry with nitrogen-vacancy defects in diamond, *Reports on Progress in Physics* **77**, 056503 (2014).
- [26] C. Slichter, *Principles of Magnetic Resonance*, Springer Series in Solid-State Sciences (Springer Berlin Heidelberg, 1996).
- [27] J. T. Oon, J. Tang, C. A. Hart, K. S. Olsson, M. J. Turner, J. M. Schloss, and R. L. Walsworth, Ramsey envelope modulation in nv diamond magnetometry, *Phys. Rev. B* **106**, 054110 (2022).
- [28] Y. Azuma, S. Nomura, H. Watanabe, and S. Kashiwaya, Angle dependence of ^{15}N nuclear spin dynamics in diamond nv centers (2023), arXiv:2306.07556 [quant-ph].
- [29] H. J. Mamin, M. H. Sherwood, M. Kim, C. T. Retner, K. Ohno, D. D. Awschalom, and D. Rugar, Multipulse double-quantum magnetometry with near-surface nitrogen-vacancy centers, *Phys. Rev. Lett.* **113**, 030803 (2014).
- [30] P. London, P. Balasubramanian, B. Naydenov, L. P. McGuinness, and F. Jelezko, Strong driving of a single spin using arbitrarily polarized fields, *Phys. Rev. A* **90**, 012302 (2014).
- [31] C. Müller, *Sensing single spins with colour centres in diamond*, Ph.D. thesis (2016).
- [32] F. Campaioli, J. H. Cole, and H. Hapuarachchi, Quantum master equations: Tips and tricks for quantum optics, quantum computing, and beyond, *PRX Quantum* **5**, 020202 (2024).

- [33] J. Johansson, P. Nation, and F. Nori, Qutip: An open-source python framework for the dynamics of open quantum systems, *Computer Physics Communications* **183**, 1760 (2012).
- [34] J. Johansson, P. Nation, and F. Nori, Qutip 2: A python framework for the dynamics of open quantum systems, *Computer Physics Communications* **184**, 1234 (2013).
- [35] D. Manzano, A short introduction to the lindblad master equation, *AIP Advances* **10**, 025106 (2020).
- [36] K. Volkova, J. Heupel, S. Trofimov, F. Betz, R. Colom, R. W. MacQueen, S. Akhundzada, M. Reginka, A. Ehresmann, J. P. Reithmaier, S. Burger, C. Popov, and B. Naydenov, Optical and spin properties of nv center ensembles in diamond nano-pillars, *Nanomaterials* **12** (2022).
- [37] G. Balasubramanian, I. Chan, R. Kolesov, M. Al-Hmoud, J. Tisler, C. Shin, C. Kim, A. Wojcik, P. R. Hemmer, A. Krueger, *et al.*, Nanoscale imaging magnetometry with diamond spins under ambient conditions, *Nature* **455**, 648 (2008).
- [38] J. M. Binder, A. Stark, N. Tomek, J. Scheuer, F. Frank, K. D. Jahnke, C. Müller, S. Schmitt, M. H. Metsch, T. Udden, T. Gehring, A. Huck, U. L. Andersen, L. J. Rogers, and F. Jelezko, Qudi: A modular python suite for experiment control and data processing, *SoftwareX* **6**, 85 (2017).
- [1] J. L. Rodgers and W. A. Nicewander, Thirteen ways to look at the correlation coefficient, *The American Statistician* **42**, 59 (1988).
- [40] N. Zhao, J. Honert, B. Schmid, M. Klas, J. Isoya, M. Markham, D. Twitchen, F. Jelezko, R.-B. Liu, H. Fedder, *et al.*, Sensing single remote nuclear spins, *Nature nanotechnology* **7**, 657 (2012).
- [41] A. P. Nizovtsev, S. Y. Kilin, A. L. Pushkarchuk, V. A. Pushkarchuk, and F. Jelezko, Theoretical study of hyperfine interactions and optically detected magnetic resonance spectra by simulation of the c291[nv]-h172 diamond cluster hosting nitrogen-vacancy center, *New Journal of Physics* **16**, 083014 (2014).
- [42] A. Dréau, J.-R. Maze, M. Lesik, J.-F. Roch, and V. Jacques, High-resolution spectroscopy of single nv defects coupled with nearby ^{13}C nuclear spins in diamond, *Phys. Rev. B* **85**, 134107 (2012).
- [43] B. Smeltzer, L. Childress, and A. Gali, ^{13}C hyperfine interactions in the nitrogen-vacancy centre in diamond, *New Journal of Physics* **13**, 025021 (2011).
- [2] Z.-Y. Wang, J. E. Lang, S. Schmitt, J. Lang, J. Casanova, L. McGuinness, T. S. Monteiro, F. Jelezko, and M. B. Plenio, Randomization of pulse phases for unambiguous and robust quantum sensing, *Phys. Rev. Lett.* **122**, 200403 (2019).
- [45] J. F. Haase, Z.-Y. Wang, J. Casanova, and M. B. Plenio, Pulse-phase control for spectral disambiguation in quantum sensing protocols, *Phys. Rev. A* **94**, 032322 (2016).
- [3] Z. Wang, J. Casanova, and M. B. Plenio, Enhancing the robustness of dynamical decoupling sequences with correlated random phases, *Symmetry* **12**, 730 (2020).
- [47] L. Tsunaki, Dataset for ambiguous resonances in multipulse quantum sensing with nvs (2024), available at: https://figshare.com/articles/dataset/Dataset_for_Ambiguous_Resonances_in_Multipulse_Quantum_Sensing_with_NVs/26245895 .

Supplementary Materials: Ambiguous Resonances in Multipulse Quantum Sensing with Nitrogen Vacancy Centers

S1. EXPERIMENTAL SETUP

The experiments were performed on a custom-made confocal microscope. A diode laser with a wavelength of 518 nm (iBEAM-SMART-515-S, TOPTICA Photonics AG) was used for both continuous and pulsed optical excitation of an NV center. Emitted fluorescence was collected either with an air objective (MPlanApo N 50 \times /0.95, Olympus) with NA = 0.95 or an oil objective (HCX PL APO 100 \times /1.40, Leica; type F immersion liquid, Leica) with NA = 1.40 and detected by an avalanche photodiode (SPCM-AQRH-14, Excelitas). The laser light was blocked from entering the detector by a 650 nm longpass filter (FELH0650, Thorlabs). Continuous microwave field for ODMR spectra was generated by a microwave source (TGR6000, TTI) and the radiofrequency signal in Sec. IV was generated by a function generator (TGF4242 LXI, TTI). Microwave pulses for dynamical decoupling multipulse sequences were generated by an arbitrary waveform generator (AWG7122C, Tektronix). In both cases generated microwave fields were amplified (ZHL-16W-43+, MiniCircuit) and then transmitted in the NV centers' proximity by a copper (99.99%) wire with a diameter of 20 μ m. Magnetic field was applied with a permanent magnet mounted on a holder with 4 degrees of freedom and with the maximum achievable magnetic field projection on NV center axis of 0.1 T. For time-resolved photon counting we used a time-correlated single photon counter (MCS6, FAST ComTec).

S2. DIAMOND SAMPLES

In Sec. IV of the main text, the effects of ^{15}N coupling on Hahn echo were measured in a IIa diamond with a ^{12}C overgrown layer of 90 nm, which was later implanted with ^{15}N at energy 2 keV and annealed at 1000 $^\circ\text{C}$ in ultra-high vacuum. For the XY8- M measurements, another shallow implanted sample was used with implantation energy 2 keV and dose 10^9 $^{15}\text{N}^+/\text{cm}^2$, annealed at 10^{-7} mbar and 1000 $^\circ\text{C}$. In Sec. V, the ^{13}C ambiguous resonance were studied in an electronic grade diamond grown by chemical vapor deposition, with natural abundance of ^{13}C and ^{14}N , in order to avoid ^{15}N effects. Finally, the ambiguous resonances from finite pulses in Sec. VI were measured in a thin electronic grade diamond plate with deeper ^{15}N implantation (20-30 keV) and doses around 10^9 $^{15}\text{N}^+/\text{cm}^2$, also annealed in ultra high vacuum at 1000 $^\circ\text{C}$.

S3. PEARSON CORRELATION COEFFICIENT

As discussed in the main text, experimental fluorescence intensity and simulated transition probability to the bright state are related through a linear equation. Therefore, an appropriate metric to determine the correlation between both is the Pearson coefficient r [S1], which is the square root of the coefficient of determination R^2 for linear relations. It is defined as the ratio between the covariance of the two data sets and the product of their standard deviations, where one data set represents the experimental data and the other the simulation. Within this definition, r is normalized from -1 to 1, with $r = 0$ representing no linear dependency between experimental and simulated data, while $r = 1$ indicates a perfect linear correlation.

To illustrate this, Fig. S1 shows simulations for XY8-2 of the ^{15}N ambiguous resonances at $B_0 = 17$ mT for different pulse length deviations in regards to the actual π -pulse duration T_p/t_π (Sec. IV of main text). Compared to the actual experimental data, assuming $T_p/t_\pi = 1$ results in a low correlation of $r = 0.555$ and thus an inadequate simulation of the experimental data, whereas taking $T_p/t_\pi = 0.826$ provides a better correlation of $r = 0.858$. In this case, the pulse length deviation affects the relative intensity of each resonance peak keeping their τ fixed, while also inducing a high frequency modulation of the signal.

S4. ^{13}C HAHN ECHO MODULATIONS

The Hahn echo signal at $B_0 = 31$ mT and $B_0 = 18$ mT for both m_s transitions are shown in Fig. S2. As can be observed, the simulations and experimental data both present the same modulation frequencies, however the amplitude of the fast modulation is smaller in the experiments. This could be related to some experimental error or some unconsidered factor in the Hamiltonian model. Nonetheless, this discrepancy does not affect the study of the ambiguous resonances and as seen in the main text, the calculated hyperfine matrix and the numerical model still reliably described them.

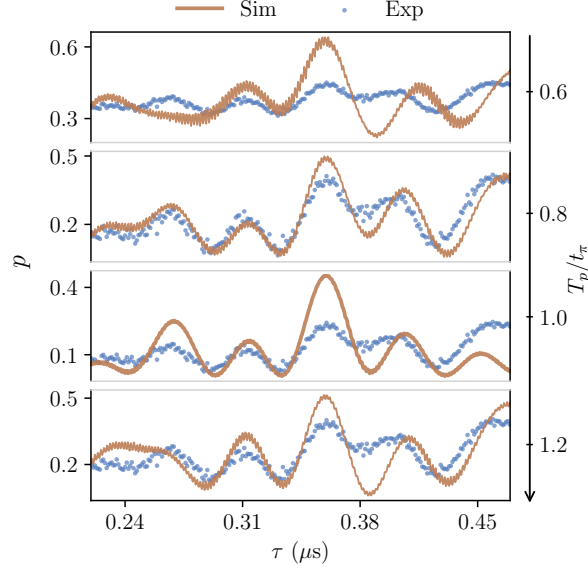


FIG. S1. The XY8-2 of the ambiguous ^{15}N resonance (Sec. IV of main text) as a function of the pulse duration T_p/t_π exemplifies the use of the Pearson coefficient, with $r = (0.419, 0.858, 0.555, 0.685)$ for $T_p/t_\pi = (0.620, 0.826, 1.000, 1.215)$ respectively. At $T_p/t_\pi = 1$ the simulated and experimental data have a poor correlation, but considering a small deviation, the experimental data can be better modeled by the simulation.

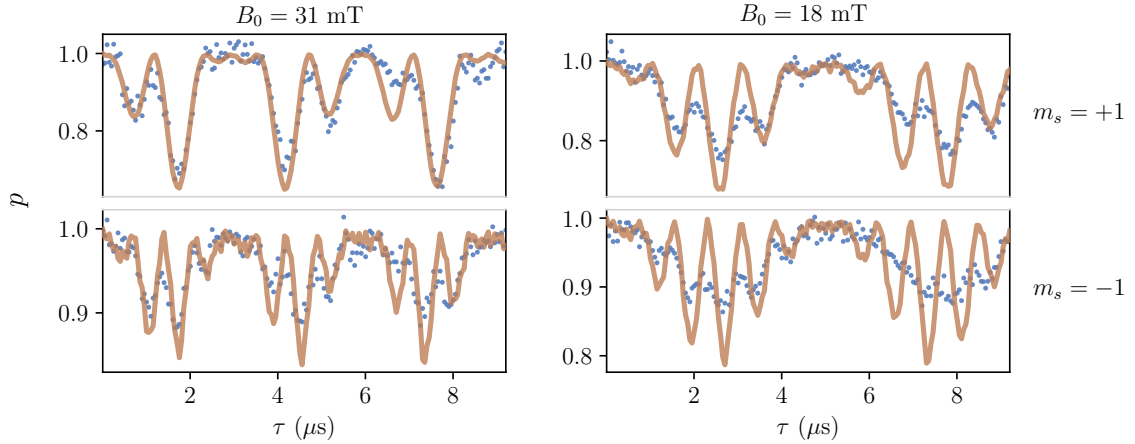


FIG. S2. Hahn echo modulations from a ^{14}NV coupled to a ^{13}C nuclear spin, resulting in correlations between experimental and simulated data of $r = (0.925, 0.792)$ at $B_0 = 31$ mT and $r = (0.806, 0.659)$ at $B_0 = 18$ mT. Although both agree in regards to the modulation frequencies, the amplitude of the faster modulation is smaller experimentally, which could be due to some experimental error or unconsidered factor in the Hamiltonian.

Based on those experimental values of the modulation frequencies, over 10^7 possible combinations of hyperfine coupling matrices between the NV and the ^{13}C nuclear spin were tested in the total Hamiltonian $H_0 + H_2$ from Eqs. 1 and 3 of the main text. The eigenenergies of the Hamiltonians were calculated numerically, with the effective Larmor frequencies $\tilde{\omega}_{m_s}^c$ corresponding to the energy differences between the carbon nuclear states in each electronic spin states m_s . The hyperfine matrix with the least square difference in units of MHz was

$$A^c = \begin{pmatrix} -0.25 & -1.85 & -0.49 \\ -1.85 & 0.00 & 0.01 \\ -0.49 & 0.01 & 1.01 \end{pmatrix}.$$

S5. PULSE ERRORS

Phase randomization can greatly increase robustness against pulse errors [S2, S3]. In non-randomized XY8, small detunings in the MW frequency δ_0 and deviations in the pulse length T_p/t_π lead to a degradation of the resonance contrast and additional peaks over the τ range, which could represent another ambiguous resonance source for similar frequency RF fields or spins. To show this effect, XY8-2 and RXY8-2 with uncorrelated phases were measured and simulated with an applied RF field of $f_0 = 5$ MHz, taking $\delta_0 = 20$ MHz and $T_p/t_\pi = 0.7$ separately (Fig. S3). Experimental parameters are $t_\pi = 15.24$ ns and $B_0 = 34$ mT with $\theta_0 = 4.1^\circ$. Again, we observe a suppression of the spurious peaks in RXY8-2 and a further validation of the simulation model. In this case at low order $M = 2$, the RF signal can be approximated by an effective hyperfine interaction with $A_{xz}^s = 0.92$ MHz and $\gamma^s B_0 = 5$ MHz, as in Eq. 4 of main text. Whereas for the higher order XY8-12 from Sec. VI of the main text, the quantum mechanical approximation of the classical RF field already deviates from the experimental data.

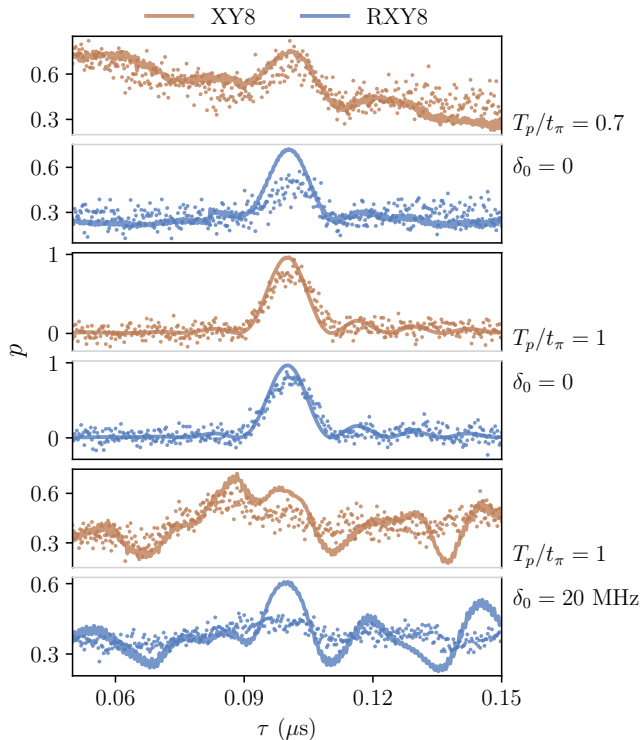


FIG. S3. XY8-2 and RXY8-2 with external RF signal of $f_0 = 5$ MHz with MW pulse deviation of $\delta_0 = 20$ MHz or length error of $T_p/t_\pi = 0.7$. The RF field is approximated by an effective hyperfine coupling with $A_{xz}^s = 0.92$ MHz, resulting in $r = (0.763, 0.907, 0.626)$ for XY8-2 and $r = (0.639, 0.915, 0.423)$ in RXY8-2. The pulse errors lead to a degradation of the contrast and additional resonances, which are suppressed by the random phases.

-
- [S1] J. L. Rodgers and W. A. Nicewander, Thirteen ways to look at the correlation coefficient, *The American Statistician* **42**, 59 (1988).
[S2] Z.-Y. Wang, J. E. Lang, S. Schmitt, J. Lang, J. Casanova, L. McGuinness, T. S. Monteiro, F. Jelezko, and M. B. Plenio, Randomization of pulse phases for unambiguous and robust quantum sensing, *Phys. Rev. Lett.* **122**, 200403 (2019).
[S3] Z. Wang, J. Casanova, and M. B. Plenio, Enhancing the robustness of dynamical decoupling sequences with correlated random phases, *Symmetry* **12**, 730 (2020).